APPLICATION AND ANALYSIS OF MICRO-CLADDING PARAMETERS FOR H13 POWDER UNDER 4340 AISI USING A FIBRE TOP-HAT LASER

APLICAÇÃO E ANÁLISE DE PARÂMETROS DE MICRO-REVESTIMENTO COM H13 EM PÓ SOB SAE 4340 UTILIZANDO UM LASER À FIBRA TOP-HAT

APLICACIÓN Y ANÁLISIS DE PARÁMETROS DE MICRO-REVESTIMIENTO PARA POLVO H13 BAJO 4340 AISI UTILIZANDO UN LÁSER DE FIBRA TOP-HAT

Paulo Paiva Oliveira Leite Dyer[1]
Maria Margareth da Silva[2]
Ana Cláudia de Oliveira Costa[3]
Joares Lidovino dos Reis[4]
Silvelene Alessandra Silva[5]
Valéria Serrano Faillace Oliveira Leite[6]
Rodrigo Cezar de Avelar Grandi[7]
Marcelo Domingues[8]
Gustavo José Lauer Coppio[9]
Luciana de Simones Cividanes[10]
Getulio de Vasconcelos[11]

Abstract: The laser micro-cladding is obtained by material deposition of interest with energy optimization aiming for a lower thermal effect, and consequently depositing a smaller and optimized structure. The technique follows the same development as laser-directed deposition (L-DED) methods. However, using boundary conditions that promote effective use of the high-energy central region of top-hat profile lasers. Therefore, this technique has a wide range of applications in engineering. However, it is still little covered in the literature, especially regarding these boundary conditions. With this in mind, this paper aimed the apply and analysis of micro-cladding parameters from previous studies. To this end, a methodological route composed of irradiation starting parameters is proposed. Next, with a deposition of one-track lines, coat-areas, and micro-additive metallurgical manufacturing structures. Using a H13 tool steel as coating powder, under discoidal substrates 25X5 mm of AISI 4340. With an experimental set-up consisting of a Ytterbium fibre laser, transported by a robotic arm, and a powder aspersing system. With this, obtained optimum parameters of the laser's power of 1300 W and velocity of scanning of 11 mm/s were obtained. The final

[1] **Instituto de Estudos Avançados. E-mail: paulo_dyer@yahoo.com**
[2] **Instituto Tecnológico de Aeronáutica. E-mail: meg@ita.br**
[3] **Universidade Federal de Lavras. E-mail: aclaudiacosta21@gmail.com**
[4] **Faculdade de Tecnologia do Estado de São Paulo. E-mail: joares.lidovino@fatec.sp.gov.br**
[5] **Instituto de Estudos Avançados. E-mail: lenisoni@uol.com.br**
[6] **Instituto de Estudos Avançados. E-mail: valeria@ieav.cta.br**
[7] **Instituto de Estudos Avançados. E-mail: rodrigorcag@fab.mil.br**
[8] **Instituto de Estudos Avançados. E-mail: marcelomd@fab.mil.br**
[9] **Instituto Federal do Estado de São Paulo. E-mail: gustavo.coppio@ifsp.edu.br**
[10] **Instituto Tecnológico de Aeronáutica. E-mail: lucianac@ita.br**
[11] **Instituto de Estudos Avançados. E-mail: getuliovas@gmail.com**

results produced structures with well-densification and superior Vickers microhardness, with metallurgical bonding.
Key words: micro-cladding; H13; AISI 4340; EHLA; Top-hat profiling; Ytterbium laser.

Resumo: O micro-revestimento a laser é obtido pela deposição de material de interesse com otimização da energia, visando reduzir o efeito térmico e, consequentemente, depositando uma estrutura menor e otimizada. A técnica segue o mesmo desenvolvimento dos métodos de deposição dirigida a laser (L-DED). No entanto, usando condições de contorno que promovem o uso efetivo da região central de alta energia dos lasers de perfil top-hat. Portanto, essa técnica tem uma ampla gama de aplicações em engenharia. No entanto, ela ainda é pouco abordada na literatura, especialmente com relação a essas condições de contorno. Com isso em mente, este artigo teve como objetivo aplicar e analisar os parâmetros de micro-revestimento de estudos anteriores. Para isso, é proposta uma rota metodológica composta por parâmetros iniciais de irradiação. Em seguida, com uma deposição de linhas de uma trilha, áreas de revestimento e estruturas de fabricação metalúrgica microaditiva. Usando um aço ferramenta H13 como pó de revestimento, sob substratos discoidais de 25X5 mm de AISI 4340. Com uma configuração experimental que consiste em um laser de fibra de itérbio, transportado por um braço robótico, e um sistema de aspersão de pó. Com isso, foram obtidos os parâmetros ideais de potência do laser de 1.300 W e velocidade de varredura de 11 mm/s. Os resultados finais produziram estruturas com boa densificação e microdureza Vickers superior e presença de ligação metalúrgica.
Palavras-chave: micro revestimento; H13; SAE 4340; ALAV; perfil Top-hat, laser de itérbio.

Resumem: El micro-recubrimiento láser se obtiene mediante la deposición del material de interés con optimización de la energía, con el objetivo de reducir el efecto térmico y, en consecuencia, depositar una estructura más pequeña y optimizada. La técnica sigue el mismo desarrollo de los métodos de deposición dirigida por láser (L-DED). Sin embargo, utiliza condiciones de contorno que promueven el uso efectivo de la región central de alta energía de los láseres con perfil top-hat. Por lo tanto, esta técnica presenta una amplia gama de aplicaciones en ingeniería. No obstante, aún está poco abordada en la literatura, especialmente en lo que respecta a dichas condiciones de contorno. Con base en ello, este artículo tuvo como objetivo aplicar y analizar los parámetros de micro-recubrimiento reportados en estudios previos. Para ello, se propone una ruta metodológica compuesta por parámetros iniciales de irradiación. Posteriormente, se realizó la deposición de líneas de una sola pista, áreas de recubrimiento y estructuras de fabricación metalúrgica micro aditiva. Se utilizó acero herramienta H13 como polvo de recubrimiento, sobre sustratos discoidales de 25 × 5 mm de AISI 4340. La configuración experimental consistió en un láser de fibra de iterbio, transportado por un brazo robótico, y un sistema de alimentación de polvo. Como resultado, se obtuvieron parámetros óptimos con una potencia de láser de 1.300 W y una velocidad de barrido de 11 mm/s. Los resultados finales produjeron estructuras con buena densificación, micro dureza Vickers superior y presencia de unión metalúrgica.
Palabras clave: micro-recubrimiento; H13; SAE 4340; ALAV; perfil top-hat; láser de iterbio.

1 INTRODUCTION

The latest trend in surface improvement and/or structural growth involves automated processes and optimizations incorporated into a range of applications, such as additive manufacturing (AM) (Wang et al., 2023). In the context of these applications, the laser cladding process (LC) stands out. According to Vilar (1999), LC processing consists of inserting the material to be deposited (in powder or solid form) directly into the focal region of the laser beam (coaxially or obliquely). This results in the simultaneous transfer of energy between the substrate and the material to be deposited. This setup assures high-quality and short-time processing of deposited structure or coating (Decker, 1995; Vilar, 1999). These factors are essential points for application in large industrial chains, due to controlled energy transference, assuring the metallurgical bonding.

In this ambit, some authors, such as Lusquiños et al. (2009), Li et al. (2021), and Sommer et al. (2021), highlight the LC-segment of laser direct energy deposition (L-DED). Li et al. (2019) explain that the L-DED's differential is attributed to coaxial insertion of material to be deposited, where, in this case, it comes in powder form or also called ‘coating-powder’. It is inserted using a gas flow directly into the laser beam's focal region. Thus, ensuring a beam energy transference of around 60-80% to the powder. With this, this system can produce better results than other LCs.

Despite its numerous advantages, Teixeira et al. (2024) highlight the undesirable thermal effect of the LCs process, such as crystallography change, oxidation, residual stresses, and others. With the defect occurring due to high metal melting temperatures propagation throughout heat heat-affected zone (HAZ) between the coating/substrate. Therefore, according to Hirata et al. (2023), the HAZ reduction control, during LC, in special L-DED processing, is welcome. As a counterpart, this reduction also may imply the reduction of sectional diffusion area ‘A_m’ (mm²) between coating and substrate, and the reduction of coat sectional area ‘A_c’ (mm²).

At this point, Reis et al. (2023) present a series of experimental precepts for HAZ and A_m reduction. To this end, the L-DED parameters of velocity of scanning ‘v_s’ (mm/s), power ‘P’ (W), and coating-powder feed rate ‘μ’ were controlled to obtain a micro-cladding, using a fibre laser with a Top-hat, based on the specific characteristics of this type of laser profile. According to Keist and Palmer (2016), and Tenbrock et al. (2020), despite the Top-hat, theoretically, uniform distribution of this energy along the entire beam area, in practice, a small Gaussian (of higher energy) in its central region. As a result, producing an extra diffusion-area ‘A_p’ (mm²) below A_c (Homburg & Mitra, 2012). Thus, as Reis et al. (2023) explain, the use of A_p as a diffusion region becomes convenient, considering target parameters.

Although it seems like a ‘cutting-edge’ technique, the micro-cladding has permeated the last 15 years, given the studies of Cai et al. (2009), Lusquiños et al. (2009), and Yao et al. (2015). With investigations of applications in: wear resistance improvements, electronic board traces, and micro additive manufacturing (MAM), aiming at the deposition of small structures with minimum laser thermal effect.

Even with significant research, micro-cladding remains largely unexplored, due to the research problem concerning the undesirable thermal effects of LC, especially L-DED. Therefore, finding ways to reduce these undesirable effects is of great scientific importance and technological application in industrial chains. This represents a ‘research problem’ in the context of a few solutions for the thermal

effects of L-DED, and therefore a research opportunity to advance in improving such processes.

Therefore, this underexplored topic offers significant research potential. In this way, the present study investigates micro-cladding parameters for producing tool steel (H13) coatings and MAM layers on AISI 4340 substrates. Next, the samples were sectioned (transversely), metallurgically prepared, analysed under an optical microscope (OM), scanning electron microscope (SEM), and Vickers micro hardness indenter. With these results, the coats and structures were evaluated for morphology aspects, layer densification, and mechanical properties.

2 EXPERIMENTAL PROCEDURES

In this experimental development, were adopted from Reis et al. (2023) and methodological route parameters, in line with previous studies. To this end, initially, one-track lines were made under 4340 AISI substrates, with only laser irradiation (Exe-1). Next, depositions of one-track lines, using H13 coating-powder (aspersion + laser irradiation) under 4340 substrates (Exe-2). Sequentially, depositions of areas (Exe-3). Finishing with MAM layers deposition (Exe-4). After the experiment, the samples' cross-sections, optical micrographs, and SEM images were plotted onto a process-chart, and then evaluated in light of the ‘experimental precepts chapter’. During this analysis, Exe-1 observations provided the parameter basis for other experiments: Exe-2 to 4. Finally, the sections were mechanically evaluated according Vickers micro hardness test (MHV). Noting that for metallographic preparation (for all Exe-1 to 4 samples), the coated and irradiated samples were transversely cut to the track (or area) direction. Next, embedded in Bakelite, sanded in the grit sequence of: 120, 220, 320, 400, 800, and 1200. After that, polished in the alumina grit sequence: 0.5 and 1 µm. And finally, chemically attacked by Nital 5 %, with application for 10 s, followed by alcohol rinsing and drying.

2.1 MATERIALS

As a coating-powder, a commercial H13 tool steel PAC1476 was used. With properties of density ‘ρ_c’ (g/cm³), particle size distribution, crystallography, and EDS properties are presented in Figure 1. As substrate, on the other hand, were used 4340 AISI discoidal pieces of 5 mm thick and 25 mm in diameter, with properties, as density ‘ρ_s’ (g/cm³), also shown in Figure 1. This material was obtained from a 1 m (total length) dowel, hot rolled and annealed (830-11°C with 20 °C/h of rate). Noting that the discs weren't previously sanded or polished, only washed with soap and water.

This preliminary analysis of the materials correctly classified the coting powder, according to the manufacturer, in terms of particle size, XRD, and SEM/EDS. It should be noted that its elongated and irregular morphology is typical of water atomization processes. Similarly, the substrate presented a hardness profile typical of AISI 4340, as well as elemental composition and microstructure.

Figure 1. Materials for coating and substrate properties. Containing: particle size distribution, X-ray crystallography (particles and substrate), SEM/EDS with elemental composition (particles and substrate), and MHV profile of the substrate.

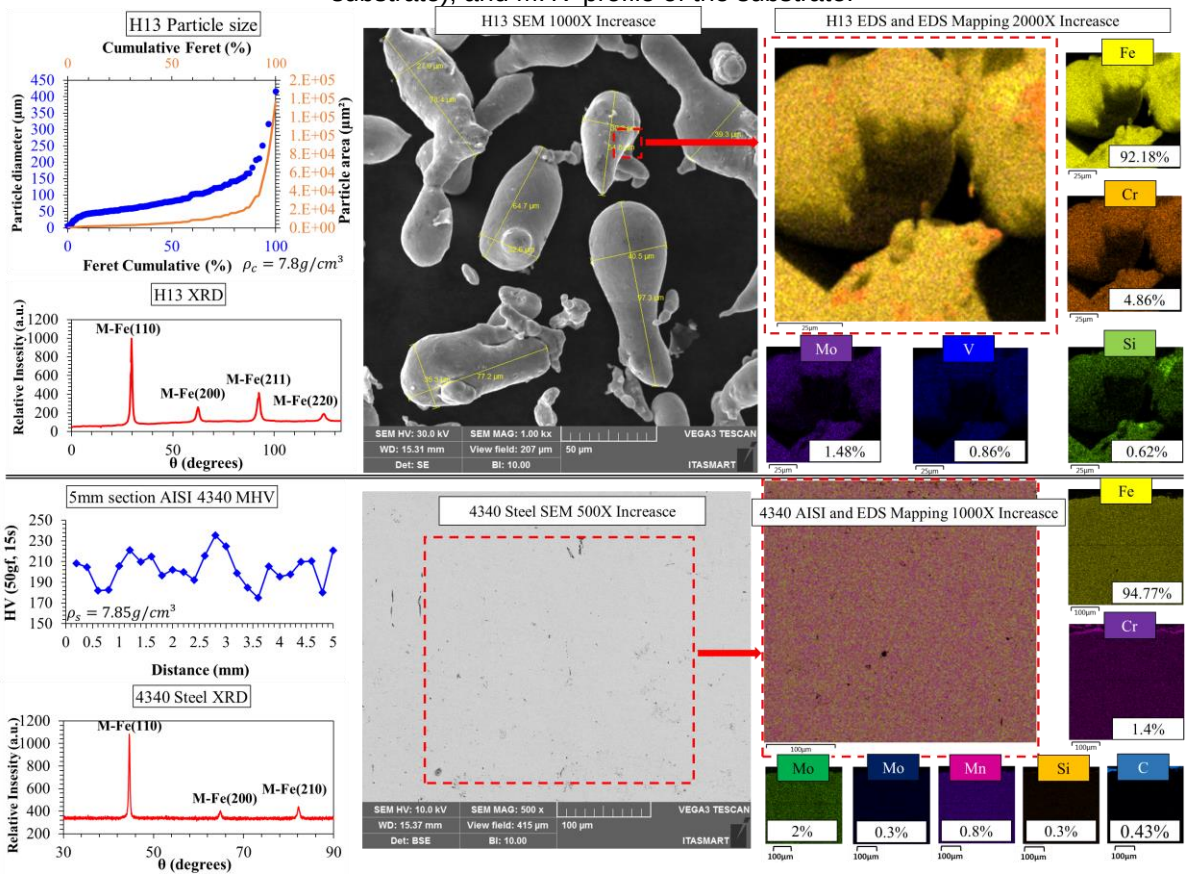

Source: Authors.

2.2 EQUIPMENT AND SUPPORT MATERIALS

The setup's experiment consisted of an L-DED system, as Figure 2. For sample preparation, on the other hand, were used: CM 60E metallographic cutter (with a T2-20441 30cm diameter diamond blade), Arotec PRE-30 embedding machine (for embedding in SOLOTEST's black Bakelite), Arotec polishing machine for sanding and polishing (with KLINGSPOR sandpaper and Arotec alumina), and Prolab Nital reagent. Next, for the analysis were used: a Zeiss optical microscope, Tecsan Vega SEM coupled to an energy dispersive X-ray spectroscopy (EDS) detector, and FM700 MHV test meter.

Figure 2. Laboratory set-up equipment. Highlights include the robotic arm system and L-DED headstock, which is controlled by predefined programming routines. The head's optics are powered by a fiber optic laser beam. In addition, there is a coating powder spraying system, coaxial with the laser's focal region.

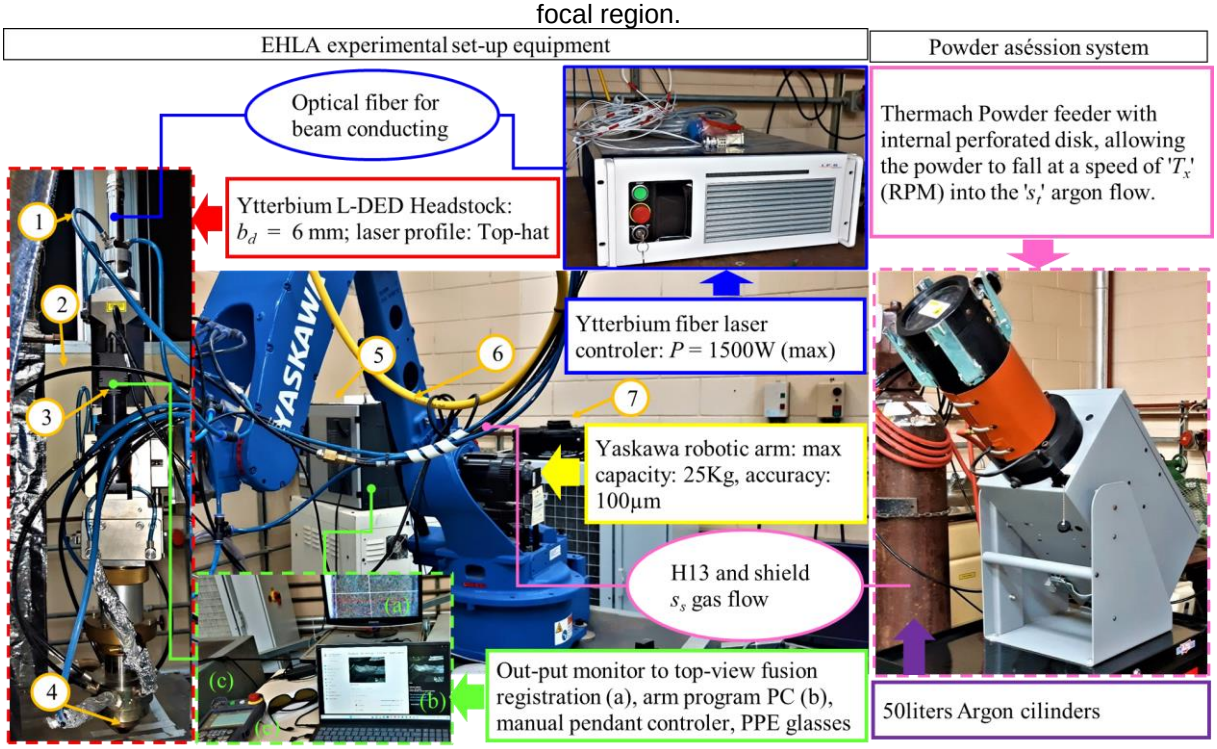

Source: Authors.

2.3 ASPERSING SYSTEM CALIBRATION

The coating-powder aspersing system, as Figure 2 briefly states, coaxially directs the powder cone into the laser focal region, as detailed by Figure 3[A]. Thus, the deposition rate μ (or amount of transported powder by time) depends on the transport Argon flow 's_t' (l/min) and the coat-powder fall rate into the s_t flow. In this case, the equipment's internal perforated disk (500 µm of hole diameters) rotates at a set angular speed 'T_x' (in RPM), allowing a controlled fall rate into the flow as Figure 3[B]. In this way, for μ calibration it's necessary the empirically collect over a given time 't' (s). Next, weighing the collected powder, and obtaining μ (g/min) for a given s_t and T_x, as Figure 3[C] graph. Where several collections at different s_t and T_x were carried out, obtaining a correlation between variables. Allowing the μ determination for each experiment.

Figure 3. Aspersing powder: [A] coaxial system, it asperges the flow of coating-powder in the focal region of the laser; [B] powder feeder, it consists of a pressurized chamber that stores the coating-powder, allowing it to 'fall' through the movement of an internal perforated disc in the argon gas flow; [C] calibration graph, this define the variation in the feed rate of the coating powder as a function of the flow and rotation speed of the internal disc.

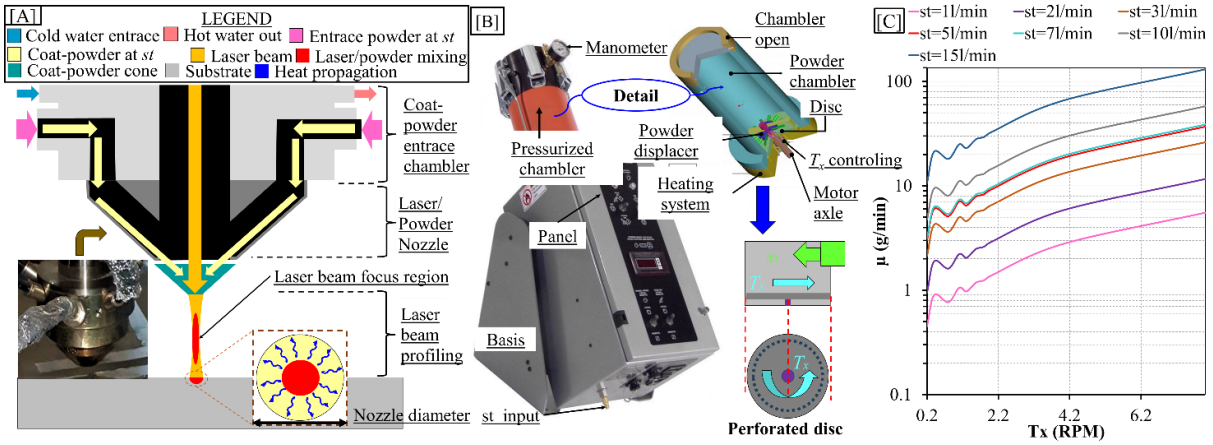

Source: Authors.

2.4 PROGRAMMING PROCEDURES AND EXPERIMENT PARAMETERS

As with the aspersing system, both irradiation and deposition processes are imbued with specificities, requiring some routines of programming for L-DED's path deposition. To this end, in parallel to μ calibration, three basic routines were implemented: one-track line (OTL) with 20 mm length, 20X5 mm area by lines overlapping (AOL), and layer growth of 20X15 mm area with 0.5 mm of thickness 'l_z' by layer (LGA). Initially, routines were developed into RoboDK software, which reproduces the real spatial conditions of the experiment regarding a 3D virtual environment, as illustrated by Figure 4[A]. Where, for each programming, a certain strategy was carried out, every maintaining a constant distance between the laser nozzle and substrate 'f_d' (mm). For OTL trajectories, the robotic arm moved linearly between points A and B. For AOL and LGA, on the other hand, the arm performed a zig-zag trajectory with 6 parallel lines with an offset of 3mm (O_v), as shown in Figure 4[C]. After this, programs were exported into robotic language (Python), as Figure 4[B] details. Therefore, in order to produce a process-chart for each Exe-1 to 4 L-DED, parameters were varied, as shown in Table 1. Where '$P_{(l)}$' is the laser power (W) with only irradiation (without coating-powder), '$P_{(\mu)n}$' (W) is the laser power with coating-powder asperging (deposition) with 'n' (T^{-1}) identifying the order of deposition power. Observing that for Exe-1, the L-DED only laser irradiated the substrate. However, for some deposition experiments, L-DED's first run was with only irradiation for substrate preheating. To this end, the program was being run for irradiation and restarted for deposition. Furthermore, for MAM, the program was interrupted at the end of the first layer for preheating. In sequence, restarted for the MAM deposition.

Figure 4. Programming procedures: [A] virtual set-up, which corresponds exactly to the laboratory environment, including the robot model and spatial location of the substrate and the tip of the headstock; [B] paths, which define the deposition path for a given experiment; [C] output Python program, which is the output program that is interpreted by the machine.

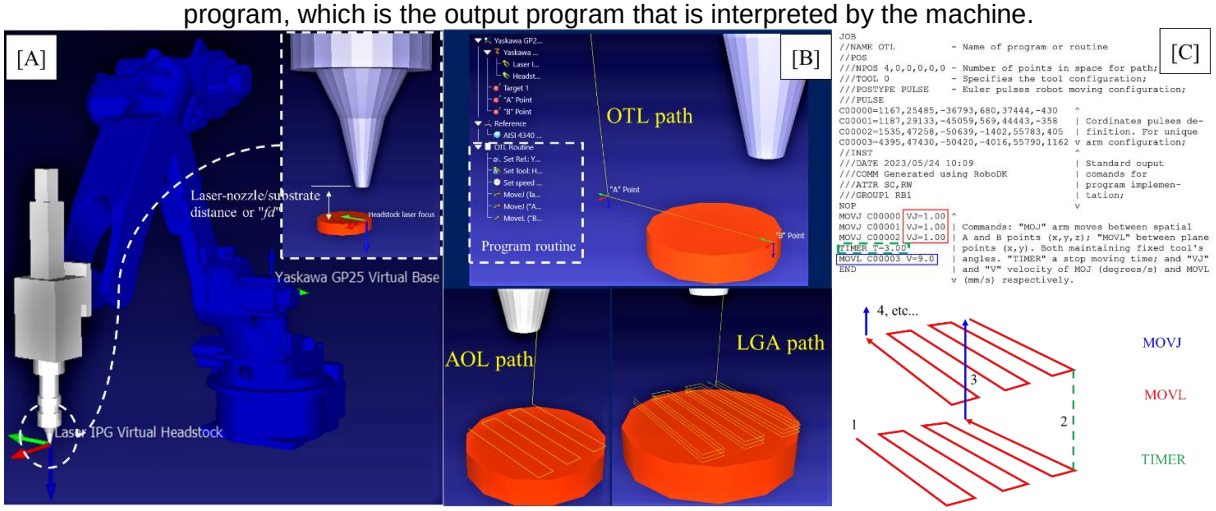

Source: Authors.

Table 1. Experiments: Exe-1 to 4 execution parameters for L-DED system.

Experiment	Parameters									
	$P_{(l)}$ W	$P_{(\mu)1}$ W	$P_{(\mu)2}$ W	$P_{(\mu)3}$ W	μ g/min	v_s mm/s	s_s l/min	s_t l/min	l_z (prog) mm	f_d mm
Exe-1a	**1032**	**-**	**-**	**-**	**-**	**25.9**	**5.0**	**5.0**	**-**	**38.0**
Exe-1b	**1032**	**-**	**-**	**-**	**-**	**18.0**	**5.0**	**5.0**	**-**	**38.0**
Exe-1c	**1300**	**-**	**-**	**-**	**-**	**25.0**	**5.0**	**5.0**	**-**	**38.0**
Exe-1d	**1300**	**-**	**-**	**-**	**-**	**18.0**	**5.0**	**5.0**	**-**	**38.0**
Exe-1e	**1300**	**-**	**-**	**-**	**-**	**19.0**	**5.0**	**5.0**	**-**	**38.0**
Exe-1f	**1125**	**-**	**-**	**-**	**-**	**5.0**	**5.0**	**5.0**	**-**	**38.0**
Exe-1g	**1032**	**-**	**-**	**-**	**-**	**5.0**	**5.0**	**5.0**	**-**	**38.0**
Exe-2a	**-**	**750**	**-**	**-**	**5.1**	**5.0**	**5.0**	**5.0**	**-**	**38.0**
Exe-2b	**-**	**803**	**-**	**-**	**7.0**	**8.0**	**5.0**	**5.0**	**-**	**38.0**
Exe-2c	**-**	**803**	**-**	**-**	**7.0**	**5.0**	**5.0**	**5.0**	**-**	**38.0**
Exe-2d	**1300**	**1300**	**-**	**-**	**7.5**	**15.0**	**5.0**	**5.0**	**-**	**38.0**
Exe-2e	**1300**	**1300**	**-**	**-**	**7.5**	**9.0**	**5.0**	**5.0**	**-**	**38.0**
Exe-2f	**-**	**1238**	**-**	**-**	**7.0**	**8.0**	**5.0**	**5.0**	**-**	**38.0**
Exe-2g	**1300**	**1300**	**-**	**-**	**7.5**	**11.0**	**5.0**	**5.0**	**-**	**38.0**
Exe-2h	**-**	**1238**	**-**	**-**	**7.0**	**5.0**	**5.0**	**5.0**	**-**	**38.0**
Exe-3a	**975**	**-**	**-**	**-**	**6.5**	**11.0**	**5.0**	**5.0**	**-**	**38.0**
Exe-3b	**1300**	**-**	**-**	**-**	**6.5**	**11.0**	**5.0**	**5.0**	**-**	**38.0**
Exe-4a	**-**	**1300**	**1300**	**1300**	**6.5**	**11.0**	**5.0**	**5.0**	**1.0**	**38.0**
Exe-4b	**1300**	**1300**	**1300**	**1300**	**6.5**	**11.0**	**5.0**	**5.0**	**1.0**	**38.0**

Source: Authors.

2.5 EXPERIMENTAL PRECEPTS

The obtained OM and SEM process-charts; from experiments cross-sections, were evaluated as whether or not as micro-cladding's experimental precepts (Reis et al., 2023). In addition, these were analysed according to an “analysis set” composed

of morphological and energy density properties (Vilar, 1999; Pellizzari et al., 2022; Dyer et al., 2024).

According to Reis et al. (2023), the micro-cladding's experimental precepts are based on L-DED parameter adjustments in order to obtain an A_p close to A_m. And thus, obtaining a controlled area of HAZ 'A_{HAZ}' (mm²) propagation, implying more effective beam-energy for coat/substrate diffusion and dilution rate 'D' (%) controlling. In this context, Tenbrock et al. (2020) highlight that, unlike Gaussian profiles, the Top-Hat, theoretically, promotes a uniform energy distribution over the entire laser-circle area (diameter of b_d), as Figure 5[A]. Although, as Homburg and Mitra (2012) explain, in practice a central-circle Gaussian energy peak promotes an extra diffusion area A_p, as Figure 5[B] diagram. Thus, once this A_p/A_m relationship is established, the analysis could be extended to a clad-morphology evaluation, according to Pellizzari et al. (2022) and Dyer et al. (2024) concepts. Where both $A_c/A_m/A_p$ ratio and A_{HAZ} morphology could be qualitatively evaluated, for each experiment, in the light of D, clad-angle 'α_c' and HAZ-angle '*Ac"* (degrees) variables, according to Equations 1 to 3. Likewise, laser beam's energy properties could be related as a function of P to the clad/irradiation's morphology and parameters of execution. In line with Vilar's (1999) and Goodarzi et al. (2015) concepts for energy density 'E_0' (J/mm²) and L-DED's track energy 'E_p' (J/mm) variables, according to Equations 4 and 5. Notwithstanding, Santos (2017) and Pellizzari et al. (2022) point out that this analysis set extends to surfaces and MAM. Observing a micro-cladding's O_v of 0%, or 3mm offset for b_d = 6 mm, as Figure 5[C]. With the variables of powder efficiency μ_p (%) and mean single-layer thickness '*Hl*' according to Equations 6 and 7.

Figure 5. Micro-cladding diagram: [A] laser profile type, and comparation to Gaussian; [B] typical clad morphology; [C] tracks overlapping scheme for area depositing O_v.

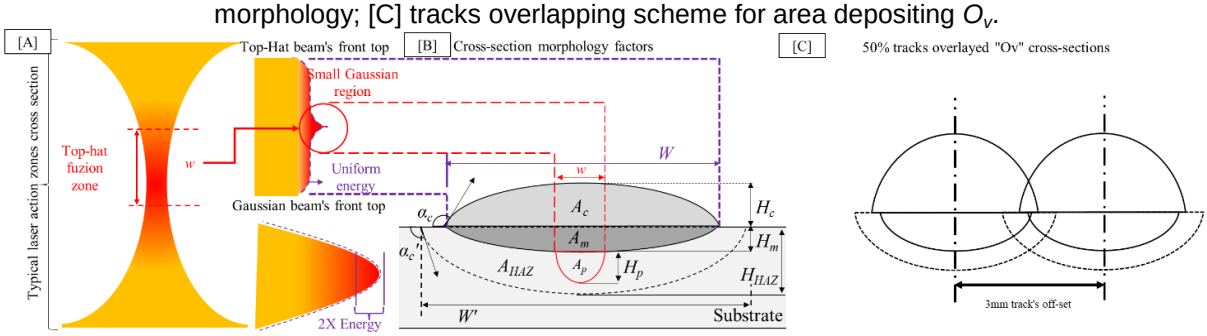

Source: Authors.

$$D = [A_m + A_p] * [A_c + A_m + A_p]^{-1} \quad (1)$$

$$\propto_c = 180 - \left|2\tan^{-1}(2H_c/W)\right| \quad (2)$$

$$\propto_c{}' = 180 - \left|2\tan^{-1}(2H_{HAZ}/W')\right| \quad (3)$$

$$E_0 = [2P] * [\pi b_d * (v_s)]^{-1} \quad (4)$$

$$E_p = 0.8[P/v_s] \quad (5)$$

$$\mu_p = [A_c] * [v_s] * [\rho_c] * [N_t * (\mu)]^{-1} \quad (6)$$

$$Hl = \left(\frac{1}{N}\right) * \left[\sum_{i=1}^{N} (H_i)\right] \quad (7)$$

3 RESULTS AND DISCUSSION

The boundary conditions of process-charts were related to v_s and P parameters for OTL programming, considering their inverse proportionality. Thus, with Exe-1's extremes discarded, was obtained balanced P/v_s for Exe-2, according to micro-cladding's experiment precepts. Similarly, this analysis was repeated from Exe-2 to Exe-3 and from Exe-3 to Exe-4. In addition, MHV analysis, coupled to process-charts, also delimited A_{HAZ} and H_{HAZ}; as well as providing information about surface improvement (or not), contributing to the best parameters determination. Likewise, the Pellizzari et al. (2022) α_c', α_c, and D boundary criteria were used as a delimiting factor for these, as a function of morphological quality. Next, Exe-2 and 3 are also evaluated in relation to elemental distribution (EDS). Finally, Exe-4's best parameters were evaluated in terms of layers densification and defects presence (OM and SEM), metallurgical bonding occurrence (EDS), and mechanical improvements (MHV).

3.1 EVALUATION OF EXE-1 IRRADIATION PARAMETERS

The main objective of micro cladding, according to Reis et al. (2023), is to determine boundary conditions for the L-DED parameters in order to concentrate the laser energy transfer near the central region of the circular beam area. Thus, obtaining an Ap corresponding to conventional Am to form a small deposited coating or structure. With this in mind, the evaluation of the HAZ produced solely by laser irradiation should aim for an AHAZ close to the center and well-defined morphology.

Figure 6 process-chart, from Exe-1a to Exe-1g, shows an increase in A_{HAZ} as a function of the increase in E_0. In this experiment, it can be seen that the delimitation of the HAZ, visually measured by AutoCAD's of OM by digitizing, and by MHV (since the laser beam creates an instantaneous hardening region in its path, increasing hardness from cementite (less hardness) to martensitic (more hardness), shows extremes (highlighted in red) that should be discarded (as already reported in the summaries in the chapter ‘Results’).

According to Vilar (1999), small A_{HAZ}s show insufficient energy transfer to melt the cladding powder and substrate, thereby preventing the anchoring of the coating or structure. On the other hand, excessive A_{HAZ}, explained by Reis et al. (2023), implies very high E0 values. These can cause excessive melting of the cladding or structure, or even cause them to vaporize. This is characterized by a wide and shallow A_{HAZ}. As a result, the desired type of structure or coating does not fit within the experimental micro-cladding precepts. Both in terms of possibly depositing a large structure or coating with many thermal repercussions, and in terms of not being able to deposit any material due to excessive vaporization of the material.

Therefore, the Exe-1 Figure 6 process-chart presents an A_{HAZ} increasing as a function of experiment development (Exe-1a to Exe-1g). Where the extremes don't present well, micro-cladding conditions. Where a little A_{HAZ} (high v_s and low P) is insufficient for cladding anchoring for metallurgical bonding. On the other hand, a great A_{HAZ} (high P and low v_s) significantly modifies the AISI 4340 microstructure; it doesn't qualify as a micro-cladding. Complementarily, the analysis set variables; as

Table 2 shows, presents an E_0 and E_p increasing, as a function of P/v_s increasing. With these considerations, Exe-1d and Exe-1e were selected as the most promising (legend in green). In this case, the α_c' of Exe-1d meets Pellizzari et al. (2022) criteria, determining a P = 1300 W and v_s = 19 mm/s for Exe-2. In fact, these parameters were closing the Reis et al. (2023) micro-cladding parameters.

Figure 6. Exe-1 process-chart for irradiation one-track lines. It contains the OM micrographs of Exe-1 ordered by the execution of each experiment (as per Table 1), together with actual measurements in microns and a graph (side view) of the MHV profile as a function of the distance between the coating surface and the substrate.

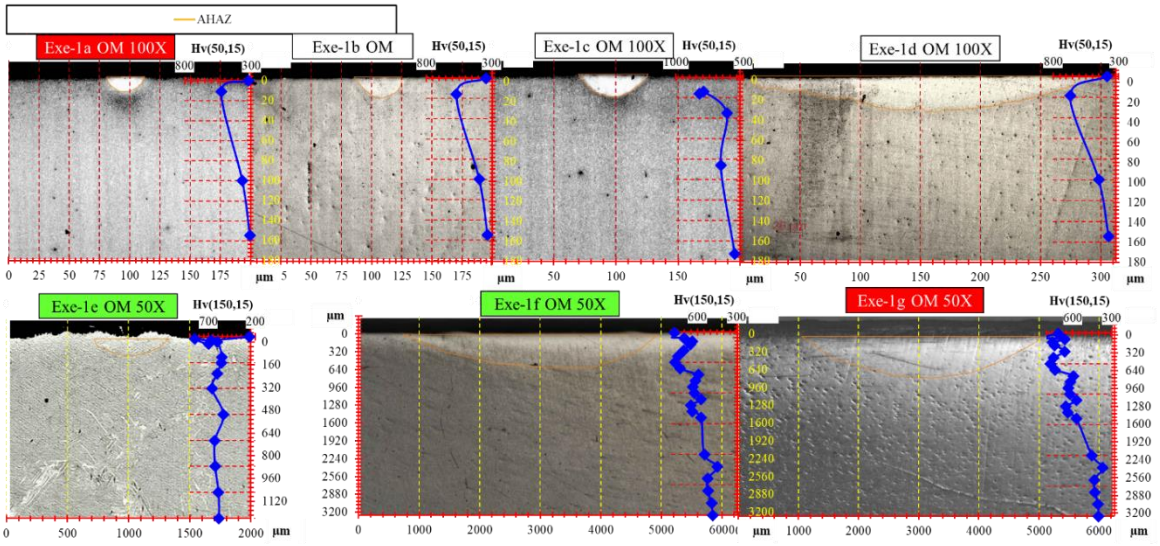

Source: Authors.

Table 2. Analyses-set variables and morphology results for Exe-1.

Exp.	W'	H_{HAZ}	A_{HAZ}	$\alpha c'$	P	v_s	E_0	E_p	v_{sc} (min)	v_{sc} (max)
	mm	mm	mm²	degrees	W	mm/s	J/mm²	J/mm	mm/s	mm/s
Exe-1a	**0.03**	**0.0003**	**0.01**	**178**	**1032**	**25**	**4.38**	**33.02**	**15**	**20**
Exe-1b	**0.04**	**0.0005**	**0.02**	**177**	**1032**	**18**	**6.08**	**45.87**	**11**	**14**
Exe-1c	**0.06**	**0.0007**	**0.02**	**177**	**1300**	**25**	**5.51**	**41.57**	**15**	**20**
Exe-1d	**0.28**	**0.0052**	**0.03**	**176**	**1300**	**18**	**7.66**	**57.74**	**11**	**14**
Exe-1e	**0.61**	**0.0589**	**0.14**	**158**	**1300**	**19**	**7.25**	**54.70**	**11**	**15**
Exe-1f	**4.26**	**1.6534**	**0.56**	**104**	**1125**	**5**	**23.87**	**180**	**3**	**4**
Exe-1g	**1.34**	**1.8841**	**0.70**	**39**	**1032**	**5**	**22.00**	**165.12**	**3**	**4**
Criteria:				**149-162**						

Source: Authors.

Furthermore, considering the L-DED's energy distribution, v_s could be refined as 'v_{sc}' of 11-15 mm/s or a P refined as 'P_c' of 1560-2080 W; according to Equation 8. However, as the IPG's maximum P is 1500 W, v_s should be the parameter to be adjusted, according to Exe-2 results.

$$v_{sc} = v_s - a * v_s;\ P_c = P + a * P; with\ a = 0.8\ (max); or\ a = 0.6\ (min) \quad (8)$$

3.2. EVALUATION OF EXE-2 DEPOSITION PARAMETERS

As Exe-1 preconized, Exe's-2 parameters of v_s = 11-15 mm/s and P = 1300 W presented the best results, as Figure 7's process-chart shows. With Exe-2d and Exe-2g (legend in green) presenting these results. Other Exe-2 experiments, such as the extremes (legend in red), on the other hand, showed an inconsistent micro-cladding's morphology (presence of great A_p, W, and A_c), or an irregular cladding (little deposition and much macro-pores presence); according morphology variables presented in Table 3. In addition, these hadn't shown MHV improvements, indicating structural defects.

Figure 7. Exe-2 process-chart for deposition one-track lines. Analogous to Figure 6, for Exe-2.

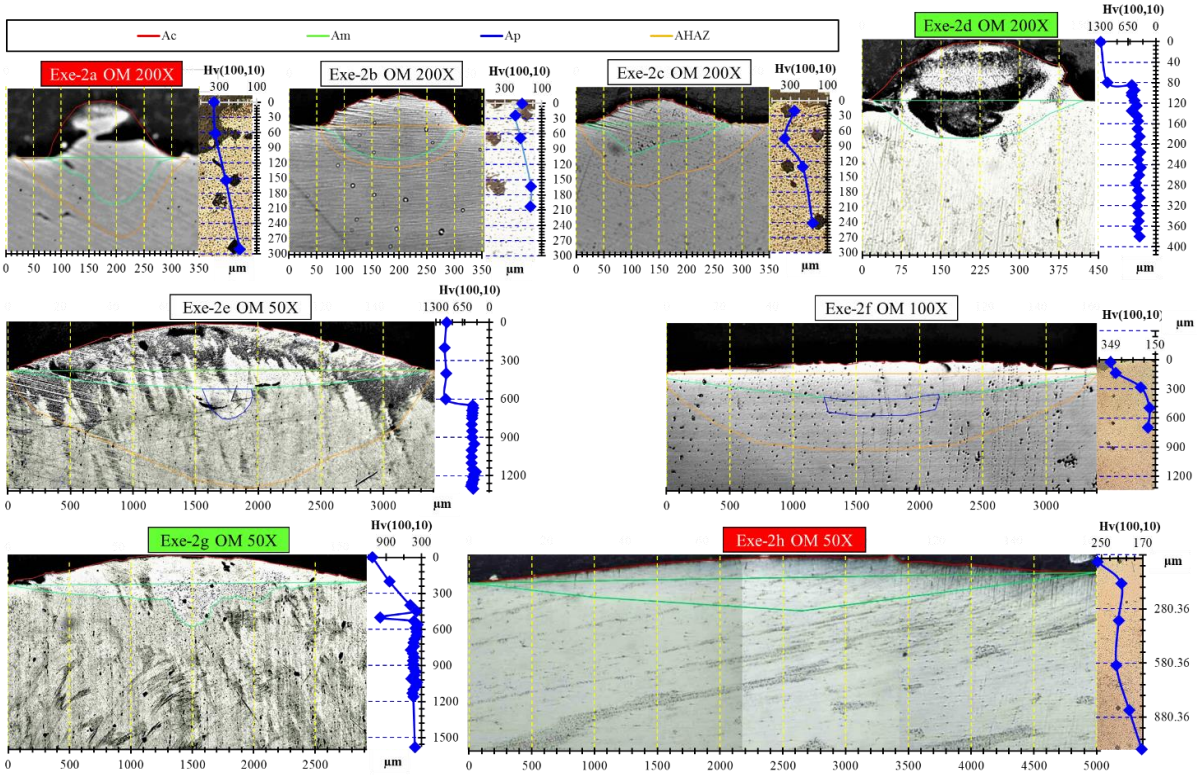

Source: Authors.

Table 3. Analyse-set for Exe's-2 morphology results.

Exp.	W mm	H_c mm	H_m mm	H_p mm	A_c mm²	A_m mm²	A_p mm²	a_c degrees	$P_{(l)1}$ W	$P_{(\mu)1}$ W	v_s mm/s	D %
Exe-2a	**0.26**	**0.11**	**0.09**	**0**	**0.02**	**0.01**	**0**	**97**	**-**	**750**	**5**	**40**
Exe-2b	**0.29**	**0.07**	**0.07**	**0**	**0.01**	**0.01**	**0**	**131**	**-**	**803**	**8**	**50**
Exe-2c	**0.27**	**0.05**	**0.06**	**0.06**	**0.01**	**0.01**	**0.01**	**140**	**-**	**803**	**5**	**66**
Exe-2d	**0.42**	**0.11**	**0.07**	**0**	**0.03**	**0.02**	**0.00**	**123**	**1300**	**1300**	**15**	**38**
Exe-2e	**3.31**	**0.37**	**0.15**	**0.24**	**0.78**	**0.32**	**0.07**	**155**	**1300**	**1300**	**9**	**34**
Exe-2f	**3.40**	**0.11**	**0.20**	**0.16**	**0.24**	**0.44**	**0.11**	**173**	**-**	**1238**	**8**	**70**
Exe-2g	**2.92**	**0.20**	**0.36**	**0**	**0.42**	**0.28**	**0**	**165**	**1300**	**1300**	**11**	**40**
Exe-2h	**5.03**	**0.16**	**0.31**	**0**	**0.49**	**0.72**	**0**	**173**	**-**	**1238**	**5**	**60**
Pellizzari et al. (2022) criteria:								**149-165**				
Dyer et al. (2024) criteria:												**38-60**

Source: Authors.

With this, Exe-2d morphology had been nearing the micro-cladding's experimental precepts, obtaining a reduced A_c without A_p. In other words, this experiment promoted an effective heat repercussion under the substrate. Similarly, these parameters improved the substrate structure with an MHV.

Complementing this analysis, Exe-2d shows a constant degree of oxidation in different regions, as shown by the EDS in Figure 8[A]. This proves a low thermal effect in this deposition, despite still showing a high degree of oxidation overall due to the action of the laser beam. This can produce a surface “scale” on the deposited material. However, this can be removed after cooling the parts by brushing-machining, a very simple finish. In contrast, Exe-2a already shows a higher oxidation content, with considerable heterogeneity of composition in different regions, as shown in Figure 8[B].

Figure 8. EDS properties of: [A] Exe-2d (coating/substrate interface), and [B] Exe-2a experiment.

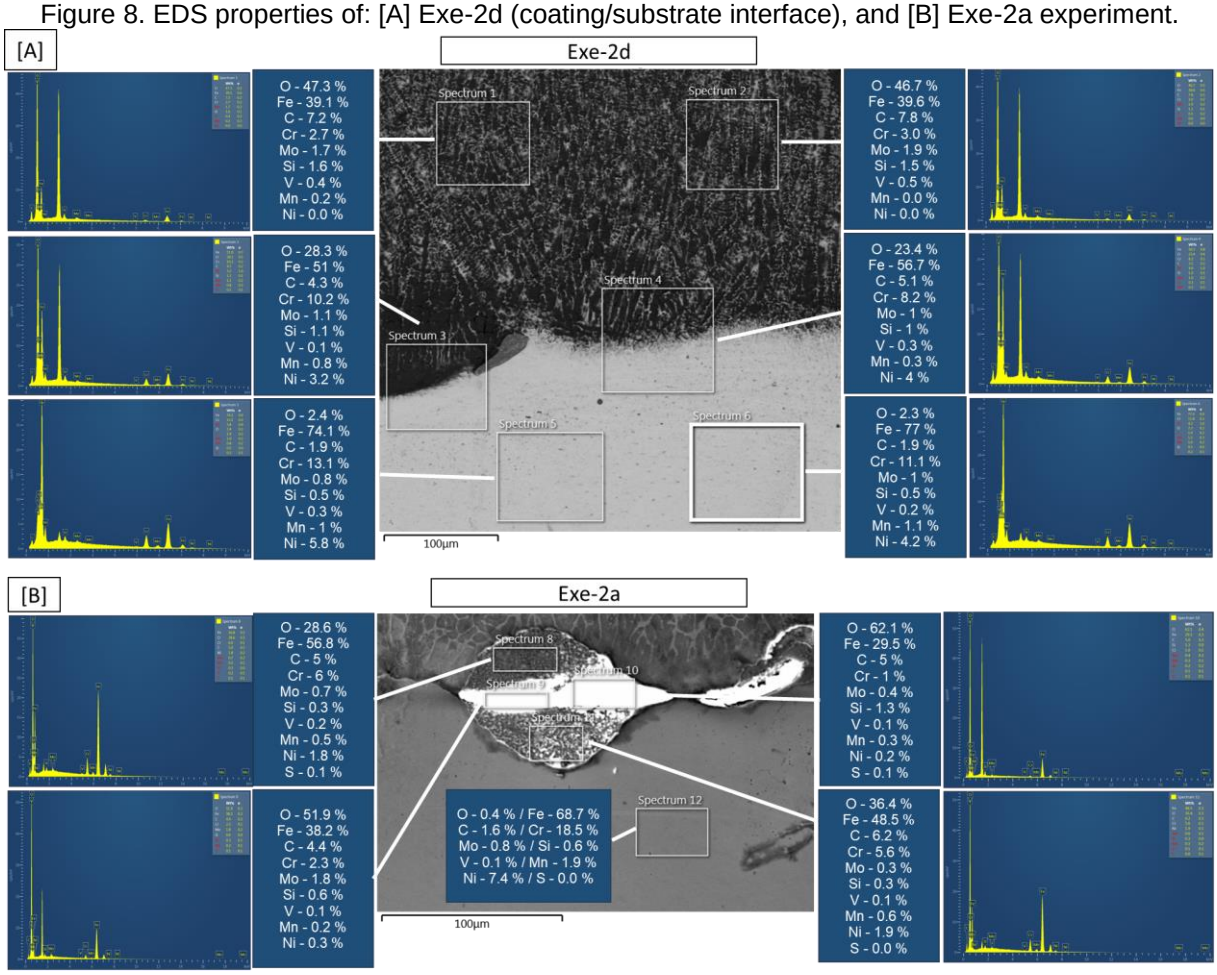

Source: Authors.

However, in Exe-2d deposition, the α_c remained outside the Pellizzari et al. (2022) criteria. Exe-1g, on the other hand, beyond presenting the same Exe-2e properties, has an α_c meeting the criteria. Furthermore, this deposition obtained an H_c and W within the program factors of I_z and lines offset, for an O_v of 0%. This makes Exe-2g suitable for surface and MAM program routines. In addition, both Exe-2d and Exe-2g met the D criteria. Dyer et al. (2024) highlight that despite many authors standing an ideal D of 8-14%, for similar coat/substrate materials (such as H13 and AISI 4340), a D value of 38-60% is acceptable. Given the greater natural

diffusion between them. This aspect was corroborated by ESD and the mapping process-chart, as Figure 9. The coloured images of the EDS map show a homogeneous mixture (observed by the interaction between the colours of the elements) between the substrate and the coating powder. Similarly, the coating is well highlighted, showing that dilution D was also not excessive, maintaining the composition of H13. And cladding morphology.

Regarding the experimental micro-cladding precepts, in addition to these morphological issues (H_c and W), Exe-2d and Exe-2g also fit the requirement of reducing thermal effects (as shown in Figure 8, for Exe-2d), characterized by a lower percentage of oxides. However, Exe-2g has an even lower oxidation content, whose distribution is uniform, as in Exe-2d (Figure 9). Thus, Exe-2g was determined to be the best parameter in the experimental stage Exe-2.

The other experiments, on the other hand, did not present satisfactory morphological aspects, in addition to not meeting the criteria of Pellizzari et al. (2022) and not obtaining an A_p replacing A_c, as in the case of Exe-2a to Exe-2c. Exe-2e and Exe-2f, on the other hand, presented high thermal repercussions. Characterized by high oxide formation (Figure 9). Exe-2h apparently did not form a cladding, with a very thin and wide structure being observed, probably due to the use of excessive E_0.

Figure 9. Exe's-2 SEM/EDS/Mapping process-chart for deposition one-track lines.

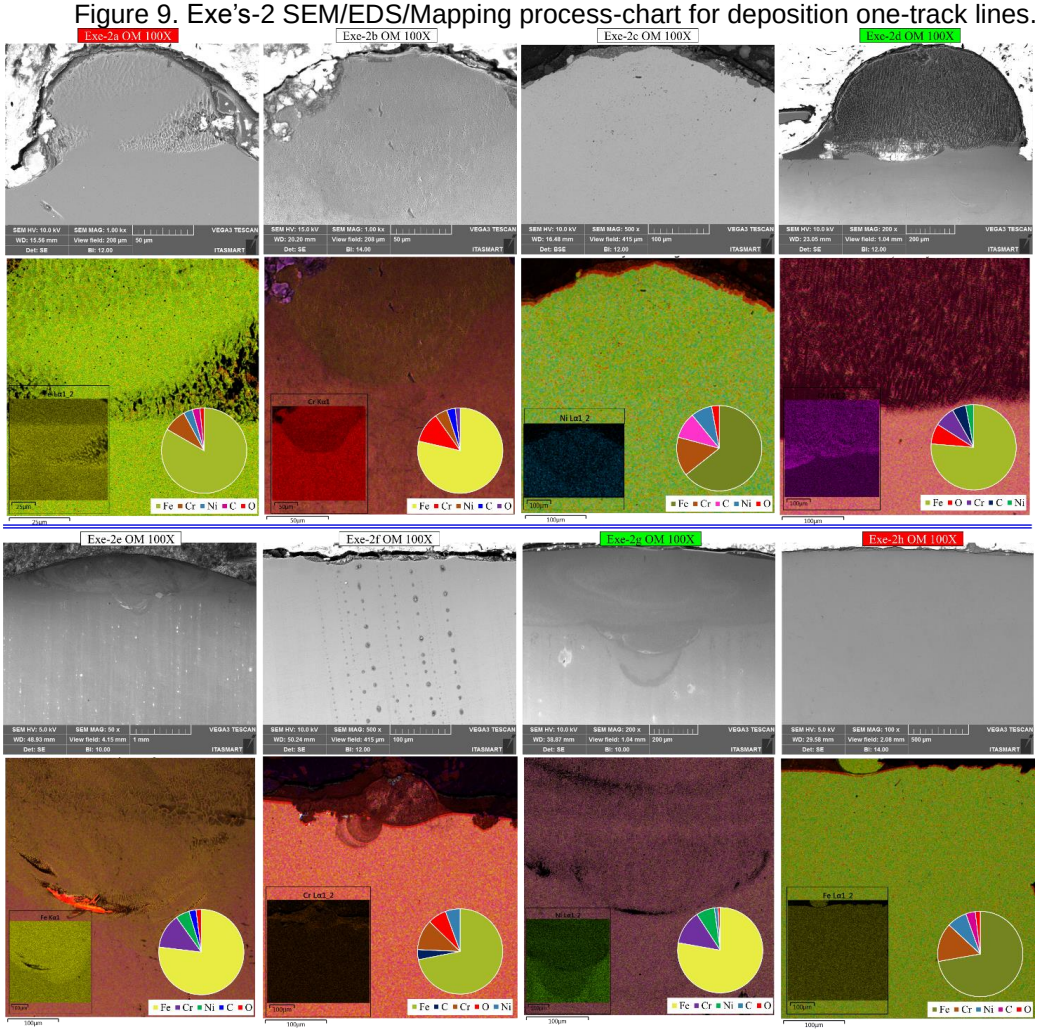

Source: Authors.

3.3 EVALUATION OF EXE-3 COAT-AREA DEPOSITION PARAMETERS

Thus, Exe-3b, which used the parameters of Exe-2d, obtained the expected properties. That is, the Exe-3 process chart confirms the observations about Exe-2, as shown in Figure 10 and Table 4, where the experiment Exe-3b had shown the best results for P = 1300 W (with substrate surface's preheating) and v_s = 11 mm/s parameters, even with a slightly lower MHV than Exe-3a.

Figure 10. Exe-3 process-chart for coat surface deposition. It contains the OM (mosaic of several micrographs) of a specific section chosen from the sample section, with actual measurements (microns). And the MHV profile in the central region.

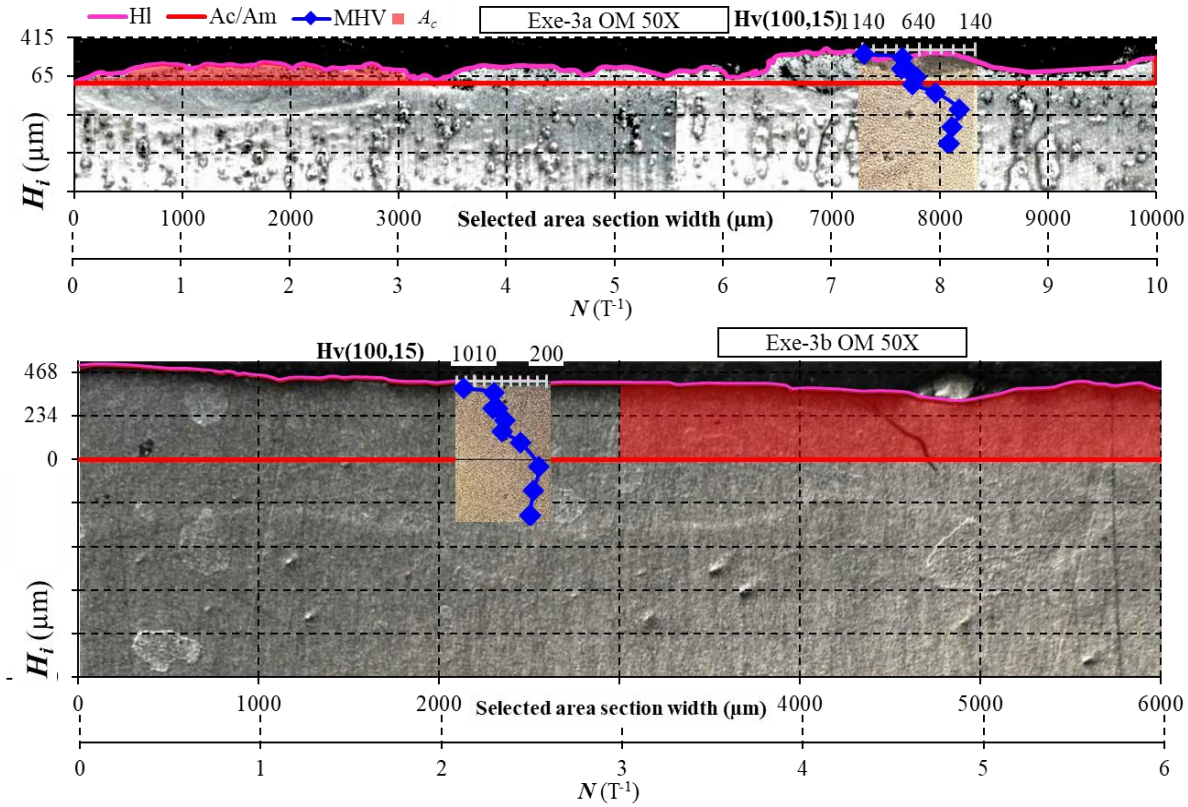

Reference: Authors (2024).

Table 4. Analyses set for morphology results for Exe-3.

Exp.	A_c mm²	v_s mm/s	ρ_c g/mm³	N_t T^{-1}	μ g/s	μ_p %	N T^{-1}	Hl mm	H_c (max) mm	H_c (min) mm
Exe-3a	**0.5**	**11**	**0.0078**	**1**	**0.1**	**35**	**10**	**0.2**	**0.3**	**0.03**
Exe-3b	**1.3**	**11**	**0.0078**	**1**	**0.1**	**98**	**6**	**0.4**	**0.5**	**0.32**

Source: Authors.

The determination of Exe-3b as the best parameter is based on morphological aspects (at a selected width of the sample section, at process-chart) and the analysis-set variables. In this context, Exe-3b had shown a median *Hl* value (0.4mm), i.e., between the maximum (0.5mm) and minimum (0.2mm). In addition, nearing the LGA's l_z (0.5mm), allowing MAM's execution. Exe-3a, on the other hand, obtained an *Hl* (0.2mm) biasing towards its maximum (0.3mm); thus, it does not maintain coherence. This explains Exe's-3b surface-coat linearity, against an Exe's-3a wavy-surfacing. Where Exe's-3b H_c variation is around 32%, compared to 91% of Exe-3a.

Concomitantly, demonstrating a fusion occurrence between AOL's 6 track-lines, even with an O_v of 0%. Exe-3a, on the other hand, had shown a surface with tracks' individual morphologies.

In Exe-3b, the effective use of E_0 may explain the uniformity of the layer height (*HI*) and fusion between the tracks that form the area coating. This is because a more regular surface deposition is observed. Thus, it can be concluded that the energy of the L-DED was able to effectively fuse the coating powder and the substrate, ensuring this homogeneity and metallurgical bonding.

In fact, the calculation of the variable up - Equation (6) - corroborates this assertion by obtaining a value of 96%. That is, in theory, there was almost 100% energy utilization of the L-DED system for Exe-3b. At the same time, it can be assumed that there was no unnecessary propagation of AHAZ, reducing the thermal effects in this experiment.

However, it was not possible to clearly map AHAZ visually using OM. However, the MHV profile shows some results, demonstrating a higher hardness in thickness proportionally equivalent to *HI*. The EDS map in Figure 11 shows a reduced oxidation content, indicating a reduced thermal effect. Similarly, Figure 11 demonstrates the occurrence of controlled diffusion between elements, with preservation of the coating, as observed in Exe-2d.

Therefore, Exe-3b presents a more effective use of E_0 without unnecessary A_{HAZ} propagation. This aspect it's also corroborated by a μ_p's high efficiency (98% against 35%) and the occurrence of greater diffusion between coat/substrate elements, as Figure 11.

Figure 11. Exe-3b SEM/EDS/Mapping process-chart: [A] SEM; [B] EDS-map; [C] EDS.

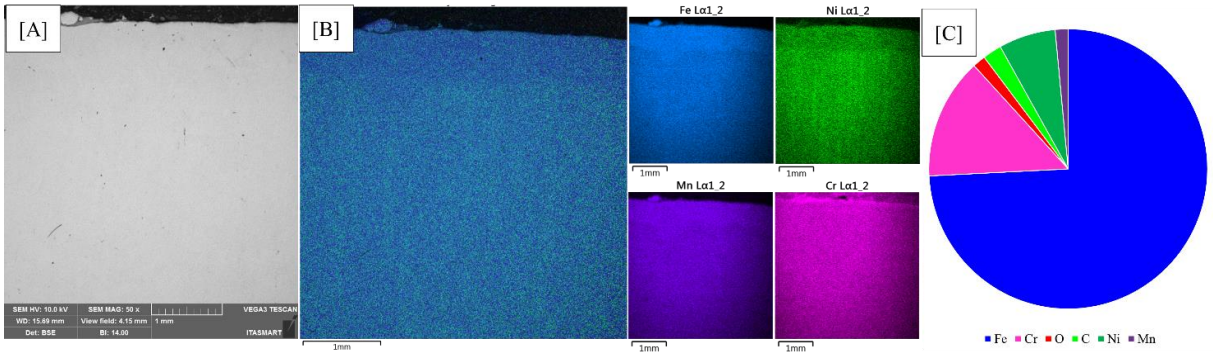

Source: Authors.

3.4 EVALUATION OF EXE-4 MAM DEPOSITION PARAMETERS

Finally, the parameters of Exe-3b applied to deposit the MAM produced a structure in Exe-4b with characteristics similar to Exe-3b. In view of the fact that in this last experiment (Exe-4), the role of substrate preheating with power $P_{(l)}$ was analysed. Thus, it was demonstrated that the crucial role of $P_{(l)}$; in substrate's preheating. As Table 5 and Figure 12 show, despite Exe-4a's same parameters as Exe-4b, this experiment didn't obtain a well-coated area fixation. As a result, a balling predominance, with no layer deposition. Where the substrate's preheating ensures the initial diffusion between coating-powder and substrate, assuring its anchoring by metallurgical bonding.

The efficiency of E_0 can also explain the need for substrate preheating applied to this parameter. Since the boundary conditions of micro-cladding limit, the use of L-

DED energy to deposit that specific amount of coating powder (determined by μ) without producing excess energy. With this, the substrate must already have a melt pool to ensure the anchoring of the first deposition layer in the MAM. This allows for better control of the quality of this deposition, according to the experimental precepts of micro-cladding, as well as the other evaluation criteria used (morphology, EDS), already predicting greater success for deposition with metallurgical bonds.

Noting that all the best parameters in the other deposition experiments (Exe-2 and Exe-3) were preceded by preheating with power $P_{(l)}$. The determination of E_0 for these experiments was based on the results observed in Exe-1. Thus, in Exe-4, the objective was to confirm this need for substrate preheating to deposit MAM.

In this context, the micro-cladding's application, using the current paper's equipment, has a narrow parameter boundary for well micro-cladding obtention. Thus, Exe-4b again confirms the P = 1300 W and v_s = 11 mm/s as the best micro-cladding's parameters; as well, the crucial role of substrate's pre-heating.

According to Figure 12's process-chart and Table 5, Exe-4b also obtained a final H_i (last layer) consistent with Exe-3b; between H_c max and min. With a final surface imbued with linearity, evidencing fusion between track lines. Likewise, the 3 layers presented a good densification between them. In addition, the Exe-4b process-chart also shows a few defects, such as macro-pores, cracks, and fissures. With an MHV profiling showed structural improvement in the H13 MAM structure.

Figure 12. Exe-4 process-chart for coat surface deposition. Analogous to Figure 10, for Exe-4.

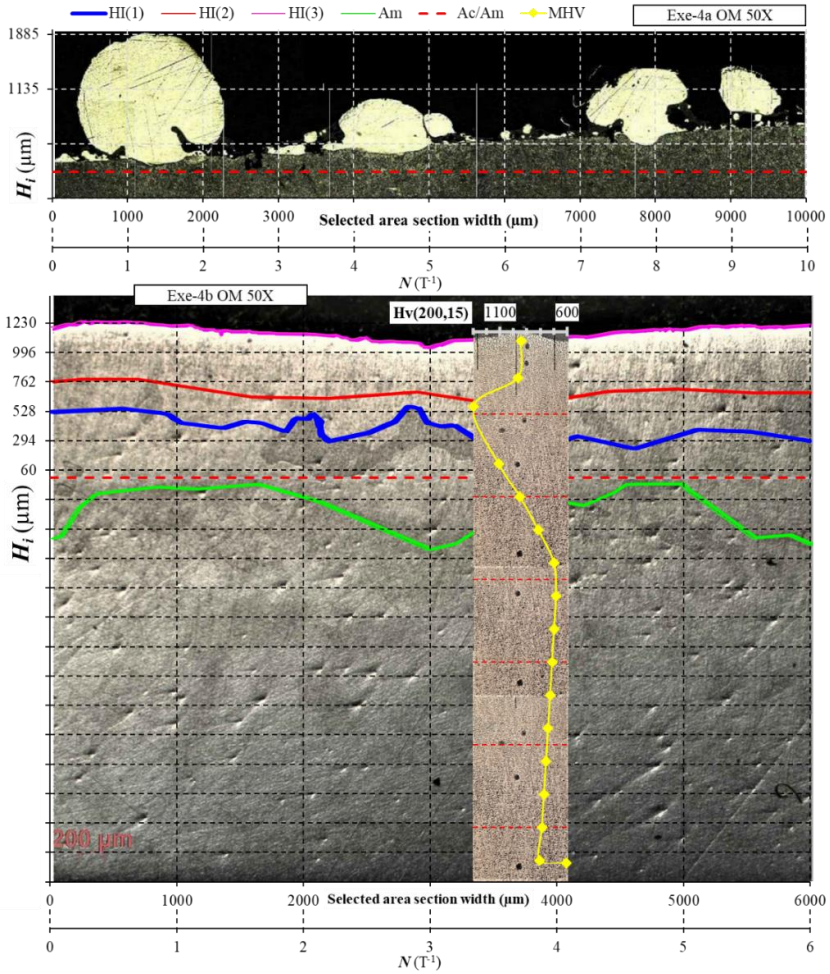

Source: Authors.

Table 5. Analyse-set for Exe-4 MAM morphology results.

Experiment:	Exe-4a					Exe-4b				
Parameters: Steps	$P_{(l)}$ W	$P_{(\mu)}$ W	*Hl* mm	*Hc (max)* mm	*Hc (min)* mm	$P_{(l)}$ W	$P_{(\mu)}$ W	*Hl* mm	H_c *(max)* mm	H_c *(min)* mm
Preheating	-	-	-	-	-	1300	-	-	-	-
Layer (1)	-	1300	-	-	-	-	1300	0.38	0.56	0.23
Layer (2)	-	1300	-	-	-	-	1300	0.28	0.47	0.10
Layer (3)	-	1300	-	-	-	-	1300	0.48	0.55	0.37

Source: Authors.

Figure 13, in turn, shows, again, a small amount of oxidation, indicating a reduction in the thermal effects of L-DED. Similarly, it shows controlled diffusion due to the homogeneity of the colours of the elements in the EDS map. As well as in the differentiation between layers. Indicating the occurrence of material consolidation between layers. This is indicative of neither absence nor excessive E_0. This is because no defects are observed, but rather a well-densified structure. At the same time, there is no excessive mixing between the layers, which maintains a linear interface surface and top line. With this, as Figure 13 SEM/EDS/Mapping process-chart shows, it isn't possible to distinguish the 3 layers' boundaries, indicating a well-diffusion occurrence between these layers by metallurgical bonding.

Figure 13. Exe-4b SEM/EDS/Mapping process-chart: [A] SEM; [B] EDS-map; [C] EDS.

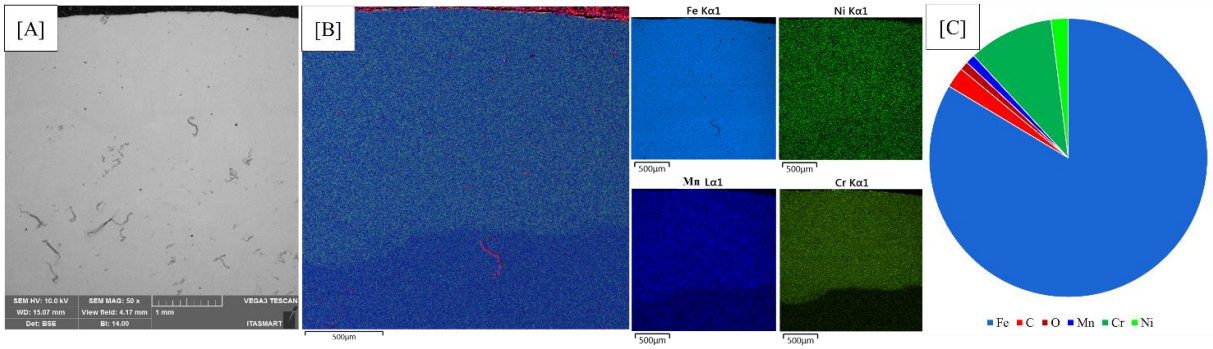

Source: Authors.

These results reinforce the applicability Reis et al. (2023) parameters for micro-cladding. To obtain MAMM structures and coatings. However, these boundary conditions, for the current equipment set-up, are very narrow-range. Therefore, the executability it's possible in terms of technical viability and operational control, although restricted.

4 CONCLUSIONS

This experimental development aimed at the micro-cladding's parameters. Considering boundary conditions for a Ytterbium fibre laser, Top-hat and b_d = 6mm; using H13 as coat-powder under AISI 4340 substrates. To this end, the developed methodological-route was imbued with starting and refinement parameters, based on previous experiments. From this development, the following conclusions were made:

a) Preliminarily, v_s = 11-15mm/s and P > 1300W parameters were accurately-obtained (for next experiments); using a process-chart of one-track irradiation

lines. Concluding that aspects of α_c', $E_{0,}$ and A_{HAZ} (according to an analysis-set variables) were being limiting factors for these parameters fixing;

b) These parameters were refined into a v_s = 11mm/s with a P = 1300W. Concluding that the morphological aspects, according to the literature, corroborate these parameters chosen. Meeting both micro-cladding's experimental precepts, cladding quality (MHV and diffusion between coat/substrate), and suitability for AOL and LGA programming;

c) Next, a new refinement, by coat-areas deposition, revealed the importance of a minimum P = 1300W setting, to assure the track-lines fusion; from AOL programming. Concluding that the reduced P using produces a wavy surface, which wouldn't meet MAMM's programming.

d) The last stage showed the substrate's preheating importance for MAM's deposition. Concluding that if this preheating was not carried out, there wouldn't be a metallurgical bonding occurrence between layers and the first-layer/substrate.

It can therefore be concluded that the above topics establish a methodical-route for determining parameters that satisfy the conditions necessary for obtaining MAM structures by micro-cladding.

In the context of this development, based on determining a parameter window to optimize the energy E_0 of the L-DED system for micro-cladding deposition. The delimitation of morphology, particularly A_m and A_p, is fundamental for diagnosing this energy effectiveness. To this end, the delimitation by digitization (using AutoCad) of such morphologies under microstructures, obtained by OM, of the cross sections proved to be efficient. This was complemented by the MHV profile. Since the rapid heating caused by the laser beam modifies the microstructure of the metal (substrate), it increases its hardness.

However, as noted in the development of the paper, other factors such as substrate preheating, become necessary to obtain the desired coating/structure. Similarly, observations regarding elemental composition, especially regarding diffusion between materials (substrate/coating powder) and oxidation, proved important in identifying the occurrence of excessive and undesirable thermal effects.

With that, parameters were determined that, at first glance, can be applied to the conditions of the tests and equipment used. However, by reducing them only to the E_0 used, they can be applied to other scenarios. They can thus be applied in other experiments, fulfilling their role in industrial chains.

5 FUTURE SCOPE

Based on this experimental development and the conclusions obtained, microcladding has a wide range of applications and new research opportunities for future studies, which should be developed in future studies, notably:

- Construction of more complex MAM structures for various applications, such as ballistic armour;
- Studies on modelling the energy of the L-DED system to further improve the efficiency of the process;
- Development of automated systems to integrate the functionalities of the robotic arm into the L-DED system to reduce deviations between experiments.

It should be noted that some of these highlights are already being developed by the same authors, notably the deposition of ballistic armour systems.

4 REFERENCES

Cai, Z., Li, X., Hu, Q., & Zeng, X. (2009). Fabrication of microheater by laser micro cladding electronic paste. *Materials Science and Engineering: B*, *157*(1–3), 15–19. https://doi.org/10.1016/j.mseb.2008.11.050

Decker, F.-J. (1995). Beam distributions beyond RMS. *AIP Conference Proceedings*, *333*, 550–556. https://doi.org/10.1063/1.48035

Reis, J., Dyer, P., Silva, S., Vicente, H., Dos Santos Paula, A., Gonçalves, D., Vieira Le Sénéchal, N., & Vasconcelos, G. (2025). Evaluation of “micro-cladding” parameters in face of thermal effects reduction for top-hat lasers. *Proceedings of the 27th International Congress of Mechanical Engineering*. 27th International Congress of Mechanical Engineering. https://doi.org/10.26678/ABCM.COBEM2023.COB2023-2231

Dyer, P. P. O. L., Silva, S. A., Oliveira, A. C. C. D., Santos, C. L. D., Vicente, H. D. P., Reis, J. L. D., Sénéchal, N. V. L., Ramos, R., Paula, A. D. S., Silva, M. M. D., & Vasconcelos, G. D. (2024). Methodology for Laser Cladding With WC and H13. *Journal of Engineering Research*, *4*(3), 2–13. https://doi.org/10.22533/at.ed.317432415019

Goodarzi, D. M., Pekkarinen, J., & Salminen, A. (2015). Effect of process parameters in laser cladding on substrate melted areas and the substrate melted shape. *Journal of Laser Applications*, *27*(S2), S29201. https://doi.org/10.2351/1.4906376

Hirata, A. K., Santos, C. L. D., Vicente, H. D. P., Dyer, P. P. O. L., & Vasconcelos, G. D. (2023). Thermal effects of AISI 304-L stainless steel after laser irradiation. *The Journal of Engineering and Exact Sciences*, *9*(11), 17806. https://doi.org/10.18540/jcecvl9iss11pp17806

Homburg, O., & Mitra, T. (2012). Gaussian-to-top-hat beam shaping: An overview of parameters, methods, and applications. Em A. V. Kudryashov, A. H. Paxton, & V. S. Ilchenko (Org.), *Proceedings of the SPIE* (V. 8236, p. 82360A). https://doi.org/10.1117/12.907914

Keist, J. S., & Palmer, T. A. (2016). Role of geometry on properties of additively manufactured Ti-6Al-4V structures fabricated using laser based directed energy deposition. *Materials & Design*, *106*, 482–494. https://doi.org/10.1016/j.matdes.2016.05.045

Li, L., Shen, F., Zhou, Y., & Tao, W. (2019). Comparative study of stainless steel AISI 431 coatings prepared by extreme-high-speed and conventional laser cladding. *Journal of Laser Applications*, *31*(4), 042009. https://doi.org/10.2351/1.5094378

Li, T., Zhang, L., Bultel, G. G. P., Schopphoven, T., Gasser, A., Schleifenbaum, J. H., & Poprawe, R. (2019). Extreme High-Speed Laser Material Deposition (EHLA) of AISI 4340 Steel. *Coatings*, *9*(12), 778. https://doi.org/10.3390/coatings9120778

Lusquiños, F., Comesaña, R., Riveiro, A., Quintero, F., & Pou, J. (2009). Fibre laser micro-cladding of Co-based alloys on stainless steel. *Surface and Coatings Technology*, *203*(14), 1933–1940. https://doi.org/10.1016/j.surfcoat.2009.01.020

Pellizzari, M., Zhao, Zhao., Bosetti, P., & Perini, M. (2022). Optimizing direct laser metal deposition of H13 cladding on CuBe alloy substrate. *Surface and Coatings Technology*, *432*, 128084. https://doi.org/10.1016/j.surfcoat.2022.128084

Santos, C. L. (2017) *Estudo do processo de sinterização/fusão de stellite 6 com laser de CO2 de 125W*. [Tese de Doutorado em Ciências e Tecnologias Espaciais. Instituto Tecnológico de Aeronaútica]. http://www.bdita.bibl.ita.br/

Sommer, N., Stredak, F., & Böhm, S. (2021). High-Speed Laser Cladding on Thin-Sheet-Substrates—Influence of Process Parameters on Clad Geometry and Dilution. *Coatings*, *11*(8), 952. https://doi.org/10.3390/coatings11080952

Teixeira, B. M. L., Dyer, P. P. O. L., Menezes, F. P., Souza, K., Guedes, V., Silva, M. M., Vasconcelos, G. (2024). Development of a Cold Spray System Applied to Coatings and Additive Manufacturing of Metals. In *Proceedings of the II Engineering Education for the Future*. Parei aqui

Tenbrock, C., Fischer, F. G., Wissenbach, K., Schleifenbaum, J. H., Wagenblast, P., Meiners, W., & Wagner, J. (2020). Influence of keyhole and conduction mode melting for top-hat shaped beam profiles in laser powder bed fusion. *Journal of Materials Processing Technology*, *278*, 116514. https://doi.org/10.1016/j.jmatprotec.2019.116514

Vilar, R. (1999). Laser cladding. *Journal of Laser Applications*, *11*(2), 64–79. https://doi.org/10.2351/1.521888

Wang, K., Liu, W., Hong, Y., Sohan, H., Tong, Y., Hu, Y., Zhang, M., Zhang, J., Xiang, D., Fu, H., & Ju, J. (2023). An Overview of Technological Parameter Optimization in the Case of Laser Cladding. *Coatings*, *13*(3), 496. https://doi.org/10.3390/coatings13030496

Yao, B., Ma, X., Lin, F., & Ge, W. (2015). Microstructure and mechanical properties of Ti-6Al-4V components fabricated by laser micro cladding deposition. *Rare Metals*, *34*(7), 445–451. https://doi.org/10.1007/s12598-015-0461-1

ACKNOWLEDGMENTS

We thank to Advanced Studies Institute and Technological Institute of Aeronautics for support team and facilities. This work was funded by CNPq, under the grant: 405624/2022-0; CAPES, under the grant: 88887.285953/2018-00, and FINEP, under the grant: 25670-SUB-1.